THE JOURNAL OF PHYSICAL CHEMISTRY C
A JOURNAL OF THE AMERICAN CHEMICAL SOCIETY

pubs.acs.org/JPCC

Article

Effects of Nonequilibrium Atomic Structure on Ionic Diffusivity in LLZO: A Classical and Machine Learning Molecular Dynamics Study

Published as part of The Journal of Physical Chemistry C virtual special issue "Machine Learning in Physical Chemistry Volume 2".

Andrew C. Grieder, Kwangnam Kim, Liwen F. Wan, James Chapman, Brandon C. Wood, and Nicole Adelstein*

Cite This: https://doi.org/10.1021/acs.jpcc.4c00171

Read Online

ACCESS | Metrics & More | Article Recommendations | Supporting Information

ABSTRACT: To improve the performance of electrochemical devices, it is essential to understand the effects of nonequilibrium motifs in solids, such as grain boundaries, amorphous phases, and highly strained regions, on atomic-scale transport and stability. Molecular dynamics simulations are used to explore the combined effect of far-from-equilibrium atomic structures and the choice of interatomic potential on ionic diffusivity predictions for $Li_7La_3Zr_2O_{12}$ (LLZO), a promising solid electrolyte for all-solid-state batteries. Amorphization and high strain are considered using both classical Buckingham interatomic potentials and machine learning force fields. We find that both crystalline expansion and amorphization tend to slow diffusion, although the different physical encodings in the two potentials impact the properties in different ways. We trace these variations to a combination of structural and transport factors, the contributions of which are deconvoluted computationally. Graph-based analysis reveals that the variations for amorphous LLZO arise from the connectivity of diffusion pathways within the predicted structures, which generally correlates with diffusivity and is notably higher for structures generated by the machine learning force fields. Our study provides additional insight into the relationship between atomic structure and diffusivity in LLZO, while also highlighting the need for care in choosing and validating potentials to simulate far from equilibrium structures.

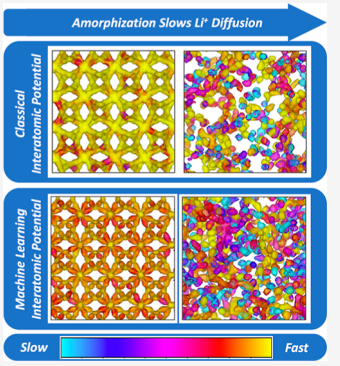

INTRODUCTION

Understanding atomic structures that lie far from equilibrium is essential to developing technologically relevant materials. Operation and processing often occur under nonequilibrium conditions, resulting in kinetically trapped metastable phases, locally strained regions, or boundary interfaces and interphases with atomic structures that do not resemble the ideal crystal. In many cases, such regions can ultimately dictate properties, performance, and lifetime of functional materials and devices. For instance, amorphous materials in energy storage devices have been shown to have desirable elastomechanical properties,[1,2] improved processability,[1,2] and better interfacial coherence and electronic properties.[3,4]

From a computational perspective, atomically disordered and strained materials have historically been especially challenging to simulate, as they require large simulation cells and many configurations for proper sampling. Molecular dynamics simulations (MD) based on ab initio calculations or interatomic potentials are widely employed to study diffusion and other dynamic atomic-scale properties in solid-state materials. However, ab initio calculations are limited by the size and time scales accessible (typically hundreds of atoms and hundreds of picoseconds), which is problematic for addressing the sampling requirements of nonequilibrium atomic structures. On the other hand, interatomic potentials have far superior scalability, but can be limited by accuracy and transferability depending on their specific validation and parametrization procedures.

Over the last several years, many researchers have selected machine-learning (ML) interatomic potentials over classical physics-based models, as ML approaches promise ab initio accuracy with high scalability. The proliferation of ML potentials has also benefited from the recent availability of many training codes.[5,6] However, whereas ML or classical interatomic potentials (CIPs) can handle size and configurational complexities, they are often parametrized for or trained on crystalline systems. Not much is known about how well such potentials perform on systems whose atomic structure lies far from equilibrium.

Received: January 9, 2024
Revised: April 26, 2024
Accepted: April 30, 2024

https://doi.org/10.1021/acs.jpcc.4c00171
J. Phys. Chem. C XXXX, XXX, XXX−XXX

In this manuscript, we systematically compare the results of simulating diffusion in disordered (amorphous) and strained crystalline systems far from equilibrium using ML versus a conventional classical Buckingham interatomic potential (CIP). We chose the garnet solid electrolyte $Li_7La_3Zr_2O_{12}$ (LLZO) as a prototypical system, focusing on the role of far from equilibrium structure in determining Li diffusion rates and mechanisms. Our aim is 2-fold: first, to provide general insights into the relationship between local atomic structure and transport behavior in LLZO, as derived from the different interatomic potential encodings; and second, to deconvolute and compare individual impacts of the two sets of interatomic potentials on predicted structural motifs versus transport behavior.

The cubic phase of LLZO[7−9] is one of the most studied solid electrolytes for all-solid-state batteries. Recently, there has been increased interest in understanding the effects of nonequilibrium motifs such as grain boundaries, amorphous phases, and highly strained regions, which appear to have non-negligible impacts both on diffusion and stability.[2,10,11] For instance, the effect of the grain structure and grain boundaries on ionic conductivity has been tested by both experiment[12,13] and computation.[14−17] These investigations have confirmed the negative impact on diffusion of atomic-scale structural disorder. However, comprehensive sampling of grain boundaries or complete disorder remains challenging to assess because of the variability of locally nonstoichiometric regions due to Li-ion segregation, various grain orientations, and potentially lower densities. Electron scattering and diffraction studies indicate that the grain boundaries in LLZO have a wide range of misorientation angles, so a particular low-angle (highly symmetric) grain boundary does not dominate the microstructure.[12,18] In addition, the width of these high misorientation grain boundaries is likely to be around 2−3 nm, which is challenging to simulate with ab initio calculations. For these reasons, in our previous study, we adopted generalized amorphous simulations as a proxy for the variety of grain boundaries in LLZO.[14] In our multiscale model of the effective diffusivity in various microstructures of LLZO, the diffusivity in the grains was set to the bulk crystalline diffusivity, while the average diffusivity at the disordered grain boundaries was parametrized by our atomic-scale MD of the diffusivity in amorphous simulations with various Li stoichiometries and densities.

These MD simulations, based on a classical Buckingham potential, exhibited a large range of local diffusion barriers, pointing to a strong coupling between local structure and transport. A follow-up study debuted a ML MD approach that was specifically trained for atomically disordered LLZO.[19]

Here we integrate and analyze those previous studies with a view toward understanding both the effects of potential choice and the specific impacts of local structural disorder on local diffusivity. In addition to amorphous structures, we include in our analysis highly strained crystalline configurations. We find that the diffusion coefficient in the crystalline systems are very similar for both potentials and match experiment, but the choice of potential significantly affects the amorphous structure and diffusivity. Our in-depth analyses and computational experiments disentangle the effect of structure versus diffusivity. In addition, we present the first atomic-scale diffusion mechanism in amorphous LLZO and identify the effect of volumetric strain on diffusivity in the crystalline phase.

METHODS

We simulated the diffusion mechanism in amorphous and crystalline LLZO at various densities and stoichiometries using the MD software LAMMPS.[20,21] For the crystalline system, we simulated the cubic phase of LLZO.[7−9] Simulations of defective or amorphous materials is challenging, especially when not much local structural information is known experimentally.[13] In particular, neutron diffraction of amorphous LLZO has not been published, so it is difficult to validate a particular potential using experimental measurements of the radial/pair distribution functions. Hence, we chose a CIP that had been demonstrated to model the crystalline system at various stoichiometries and phases,[22] as well as our trained ML potential,[19] to determine the effect of potential on the amorphous structure generation and the diffusivity.

The CIP was adopted from the study by Kozinsky et al.[22] and consists of a Coulomb interaction and a short-range Buckingham potential for the Li−O and O−O interactions[23] and La−O and Zr−O.[24] These prototypical CIPs are suitable for simulating the nonstoichiometries possible in grain boundaries because they were used by Kozinksy et al. to understand the effect of nonstoichiometry in crystalline LLZO on Li-diffusion.[22] They approximate the diffusivity and activation energy of cubic and tetragonal LLZO very well but the authors note "due to the approximate potentials and non-stoichiometric compositions used, the absolute values are not expected to describe the actual diffusion coefficients quantitatively; only qualitative comparison... is... relevant".

The ML potential was taken from our previous study by Kim et al.[19] It is based on the neural network approach with the Behler−Parrinello radial and angular atom-centered symmetry functions as atomic descriptors using the n_2p_2 code.[6,25] The ML model was trained on amorphous and crystalline structures (5500 configurations in total) from ab initio MD simulations and was validated by benchmarking properties of LLZO as well as energies and forces of MD snapshots against ab initio calculations. We found that the ML model can predict accurate structural, vibrational, and dynamical properties for crystalline as well as amorphous (completely disordered) LLZO close to those calculated by AIMD simulations, whereas amorphous properties predicted by the CIP deviated from the AIMD simulations.[19] We performed additional tests to validate the applicability of this ML model for the purpose of this study and found that our ML potential predicts accurate forces and vibrational characteristics (comparable to ab initio calculations) in LLZO systems with a range of Li concentrations and densities; see Supporting Information for detailed validation results.

In our models, we did not explicitly include dopant atoms, which are typically needed to stabilize the cubic structure, resulting in a Li-deficient stoichiometry. Since there are numerous factors that could lead to stoichiometries in the disordered grain boundaries that differ from the bulk, we deliberately chose not to include charge-compensating defects or dopants. Two previous papers provide the precedent for our methodology.[17,22] In addition, these dopants or defects would change the underlying structure of each Li-concentration, disrupting the percolation pathways, as demonstrated in a study that showed W^{6+} doping on Zr^{4+} sites impedes Li diffusion.[26] Instead, we varied the Li concentration by intentionally introducing vacancies, so the underlying strain

https://doi.org/10.1021/acs.jpcc.4c00171
J. Phys. Chem. C XXXX, XXX, XXX−XXX

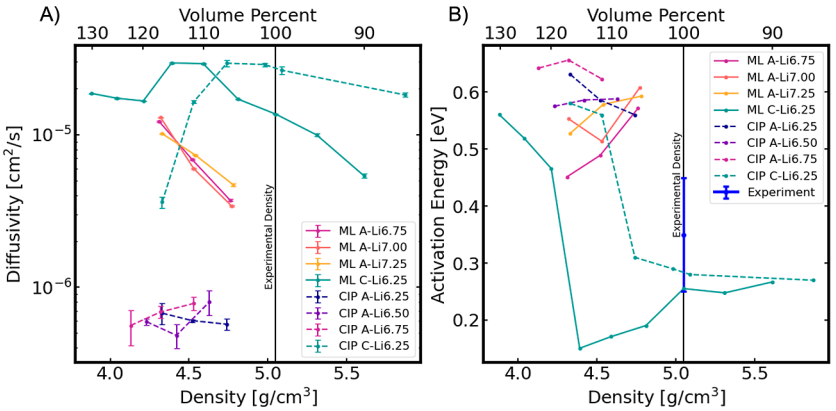

Figure 1. Lithium concentrations are presented as Li_X for X in $Li_XLa_3Zr_2O_{12}$ and the amorphous systems are abbreviated A and crystalline are abbreviated C in the legend. (A) Diffusivity for amorphous and crystalline systems at 1100 K. The experimental density for the crystalline system is 5.05 g/cm^3. (B) Activation energies calculated from Arrhenius plots of diffusion for various cell densities in the temperature range of 700−1700 K for CIP and 700−1300 K for ML potentials. Experiment represents average of experimental E_a's.[14]

or disorder in the structure could be isolated as a variable. The ML simulations included one off-stoichiometry with excess Li, which is possible in the grain boundaries.[15,27] Amorphous LLZO systems with three different stoichiometries were generated as detailed in the following section. Recall that the amorphous models can be considered as a proxy for highly unstructured grain boundaries and disordered interface regions.

MD simulations for all systems were run for 6 ns with 1 fs time step at 700−1700 K with increments of 200 K under the *NVT* ensemble using the Nosé−Hoover thermostat. In order to obtain diffusion parameters, the last 5 ns were used to calculate the mean squared displacements. Atomic positions were recorded every 200 fs. For the more detailed jump analysis, an additional 100 ps of MD were run, with positions recorded every 50 fs.

Structure Generation. The amorphous 2 × 2 × 2 supercell (1520 atoms) was generated through a melt quench procedure. Using the CIP, the $Li_{6.25}La_3Zr_2O_{12}$ unit cell was melted at 3000 K. Melting was confirmed by the formation of lanthanum and zirconium Frenkel defects. Then a melted 2 × 2 × 2 supercell was constructed and *NVT* MD were run for 1 ns at 3000 K before the cell was quenched to 500 at 5 K/ps. The cooling rate that we chose is commonly used in the literature with ab initio[28,29] melt-quench simulations. We do not expect that a slower cooling rate would result in radically different structures based on the literature, which showed that their amorphous oxide structures did not change significantly with cooling rates of 10^{13} K/s or slower using a CIP.[30] Pair distribution functions (example of Zr−Zr in Figure S11 in the Supporting Information) and coordination numbers (Figures S12−S14) show the quenched structures are significantly different than the liquid-melt, which we also quantified using a graph-based unsupervised neural network algorithm (details and Figure S7 in the Supporting Information).

After quenching the supercell, the atomic positions were used to generate the other lithium concentrations and densities. In order to increase the Li concentration by adding lithium ions into the amorphous supercell, sites were identified using analysis of the MD with the Sitator package.[31] To generate the concentrations of $Li_{6.50}La_3Zr_2O_{12}$ and $Li_{6.75}La_3Zr_2O_{12}$, lithium was added to sites in the quenched supercell to maximize the distances between lithium. Next these amorphous simulation cells were expanded to ∼105, 110, and 115% of the experimental crystalline volume (V_{exp}) for each concentration, while maintaining relative atom positions.

When using the ML potential, the initial configuration of the amorphous $Li_7La_3Zr_2O_{12}$ unit cell was generated by expanding an amorphous unit cell model built by ab initio MD in our previous study[19] with a lattice parameter of 13.5 Å. Then, a 2 × 2 × 2 supercell was constructed by repeating the expanded unit cell, which was again equilibrated at 3000 K for 100 ps with 0.5 fs time step using *NVT* ensemble followed by a relaxation of ions and cells (the cell shape was maintained as cubic during relaxation). The lattice parameter of the final amorphous supercell was 27.027 Å. We acknowledge that there are minor differences in the procedures for generating the amorphous supercells between the CIP and ML potential, but do not believe there is a significant effect on the resulting structures, as we detail in the Results and Discussion and Supporting Information.

Our analyses focus on the relationship between local structure and diffusivity, including the local jump frequencies, so will highlight any differences between the potentials.

Site Network Analysis. To investigate Li jumps, the Li sites and site networks (connectivity) were identified using the analysis software Sitator,[31] which was also used to calculate Li accessible site volumes, site residence times, and diffusion pathways. The accessible site volume is the hull volume of the Li positions when Li atoms are assigned to that site. The residence time is the length of time that a Li occupies the site. In addition to the accessible site volume calculated by Sitator, Zeo++[32] was used to calculate the volume of the sites in the amorphous and crystalline systems. The Li are removed from the sites and the nonlithium sublattice is used to calculate free site volume for lithium. The Shannon radii (Zr = 0.86 Å, O = 1.24 Å, La = 1.30 Å, Li = 0.59 Å) were used when calculating the site volume. These two different methods led to different site volumes and insights into Li behavior in various sites, as described in the last two subsections of the Results and Discussion.

Graph Order Parameter. Disordered structures were characterized using a graph order parameter (GOP) scheme[33] that aims to compare the various subgraphs contained within a system. Here, nodes in the graph represent sites that can be visited while edges represent a scenario in which a diffusion event from site *i* to site *j* occurred. The edge weights were determined by calculating the likelihood of a diffusion event

https://doi.org/10.1021/acs.jpcc.4c00171
J. Phys. Chem. C XXXX, XXX, XXX−XXX

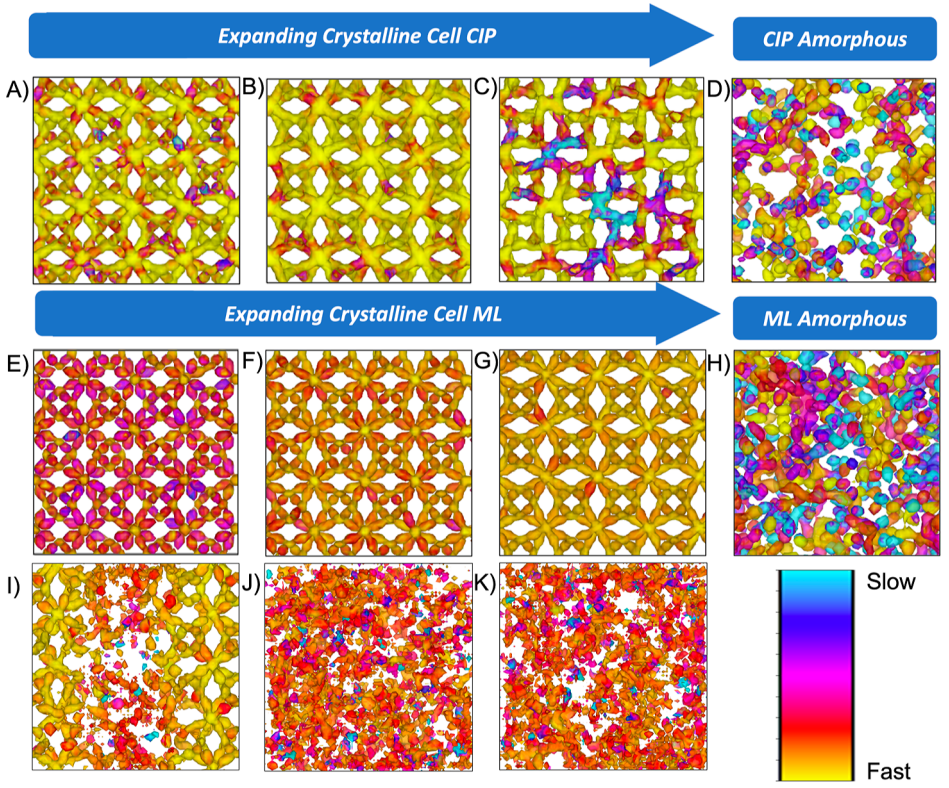

Figure 2. Lithium probability densities with color indicating the residence time of the Li site. Short residence times are fast sites and long residence times are slow sites. Bottom row highlights amorphization in the ML's nominally crystalline systems when the simulation cell is expanded from 120%V_{exp} (ρ = 4.20 g/cm^3, right) to 130%V_{exp} (ρ = 3.88 g/cm^3, left).

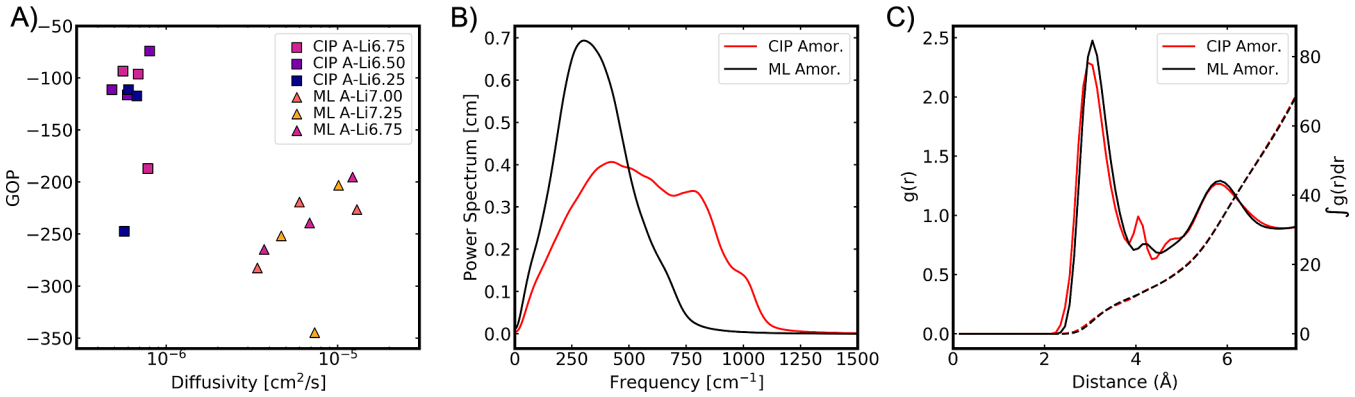

Figure 3. (A) GOP for CIP and ML amorphous (A) simulations at three densities calculated from graphs of the probability of moving from one site to the other. Probabilities and diffusion are for simulations at 1100 K. (B) Oxygen power spectrum for representative amorphous structure. (C) O−O pair-distribution function for representative amorphous structures.

occurring between sites i and j. Using this definition, the node degrees were calculated as the sum of off edge weights into a node, normalized between 0 and 1. The GOP is then calculated as

$$\theta = \sum_{s}^{S} \left(\sum_{m}^{D} P(d_m) \ln[P(d_m)] + d_m P(d_m) \right)$$

where S is the list of all subgraphs in the structure, indexed by s, D is the set of unique node degrees within the subgraph, indexed by m, d_m is a specific degree in D, and $P(d_m)$ is the probability of that degree occurring over all degrees in the subgraph.

Simulation Notation. We generated strained crystalline and amorphous structures with the CIP and ML potentials and then ran various simulations with those structures, including using a different potential for the MD than the potential that generated the structure. To distinguish between all these computational experiments, we adopt the following notation. For a given property, such as the diffusivity, D, we write A-$D^{\mathrm{ML}}_{\mathrm{CIP}}$ to indicate the structure is amorphous (A-) and the structure was generated by the CIP (subscript) while the MD was run with the ML-potential (superscript). If the same potential that generated the structure was also used to run the MD, we sometimes only employ the superscript.

https://doi.org/10.1021/acs.jpcc.4c00171
J. Phys. Chem. C XXXX, XXX, XXX−XXX

RESULTS AND DISCUSSION

Diffusivity, activation energies (E_a), lithium site volumes, Li residence times, and diffusion pathways were calculated and identified for the amorphous and crystalline systems. As expected, the crystalline simulations at the experimental density do a reasonable job of reproducing the experimental activation energy of around 0.35 eV[14] with both potentials: C-E_a^{CIP} = 0.29 eV and C-E_a^{ML} = 0.25 eV, as seen in Figure 1B (ref 14 includes a comprehensive compilation of experimental values). The amorphous simulations and strained crystalline cells with significantly higher or lower density than experimental density were found to have slower diffusivity across all systems investigated. In both cases the reduction in diffusivity is likely caused by disruption of the well-connected diffusion network present in the crystalline structure at the experimental density and local structural disorder. The ML and CIP simulations differ in the level of network disruption introduced by straining the volume of the simulation cell, as quantified by a GOP (see Figure 3A). By disorder, here we mean distorted bond angles and lengths compared to the ideal crystal structure, in addition to some Frenkel-type defects. Some far from equilibrium expanded volumes become amorphous (completely disordered) while other systems have pockets of disorder, as described below. The differences in structure connectivity, diffusivity, and the dependence on strain highlight the importance of choosing or developing accurate interatomic potentials when investigating diffusion in amorphous materials.

Our in-depth analysis of the diffusion mechanism and the jump frequency from each site gives insight into trends in the diffusivity with respect to strain and disorder. The Results and Discussion section is organized as follows: first we show the faster diffusivities in the ML versus the CIP amorphous simulations are affected by the connectivity of the ML amorphous structure, quantified using a GOP, then the inherent characteristics of the potential are distinguished from the higher connectivity of the structure made by the ML potential, and finally the effect of site volume and disorder is correlated with jump frequency.

Diffusivity and Activation Energies. We compare diffusivities in Figure 1 at 1100 K for simulations of all strained crystalline and amorphous systems (diffusivities at other temperatures are given in the Supporting Information; we highlighted 1100 K to guarantee sufficient jump statistics). In the crystalline simulations, the fastest diffusion rate was observed for cells with density slightly lower than the experimental density of 5.05 g/cm^3, for both CIP and ML potential. In particular, the CIP simulations have the maximum diffusion rate of C-D_{CIP}^{CIP} = 2.94 × 10^{-5} cm^2/s at 107% expansion of the experimental volume—V_{exp} (ρ = 4.74 g/cm^2), while the ML's maximum diffusivity is C-D_{ML}^{ML} = 2.95 × 10^{-5} cm^2/s at 115%V_{exp} (ρ = 4.39 g/cm^2). Thus, the maximum diffusivity at 1100 K agrees well between ML and CIP simulations, but the volumetric expansion associated with the maximum diffusivity value is larger for the ML simulation. The diffusivity in the CIP simulations continues to decrease with expanded volumes, such that the slowest diffusion rate of C-D_{CIP}^{CIP} = 3.61 × 10^{-6} cm^2/s occurs at the largest volumetric strain of 117%V_{exp} (ρ = 4.33 g/cm^3), among the simulations that were run.

The ML simulations similarly exhibit a maximum diffusivity before decreasing at larger volumetric strain. Slower diffusion at larger volumetric strain, although uncommon in most materials, is often seen in superionic conductors as the expansion disrupts the close interaction between the diffusing species and its atomic environment, as well as the atomic structure of the lattice itself, both of which are critical to maintaining fast conduction. In the ML simulations, we also find that the trend with increased volumetric strain ceases at 120%V_{exp} (ρ = 4.21 g/cm^3), below which there is little change in the diffusivity. The different trend for the ML systems at large volumetric strains can be explained by the amorphization of the simulation cell, while the CIP simulation cells do not become amorphous, only locally disordered. The following sections will clarify the diffusivity differences between the ML and CIP based on types of disorder created at large volumetric strain.

In both CIP and ML crystalline simulations, diffusion also slows with compressive volumetric strain (more steeply for ML than for CIP). This trend is expected, as narrower channels can impede Li diffusion. For the CIP simulations, increasing compressive strain from 107%V_{exp} (ρ = 4.74 g/cm^3) to 86% V_{exp} (ρ = 5.87 g/cm^3) decreases the diffusivity only slightly from C-D_{CIP}^{CIP} = 2.94 × 10^{-5} to 1.82 × 10^{-5} cm^2/s, while for the ML systems the diffusivity decreases significantly from C-D_{ML}^{ML} = 2.95 × 10^{-5} to 5.36 × 10^{-6} cm^2/s as compressive strain goes from 115%V_{exp} (ρ = 4.39 g/cm^3) to 90%V_{exp} (ρ = 5.61 g/cm^3). As we will explore further below, while both CIP and ML simulations have narrower channels with compressive strain, in the ML simulations all the sites become slower (see discussion around Figure 2). In the higher compressive strain CIP simulations there are still some sites that maintain fast diffusion, which mitigate the effect of the slower sites.

The differences in the amorphous systems at 1100 K between the two sets of potentials are even larger than the crystalline simulations. The diffusivity in amorphous CIP simulations is almost 2 orders of magnitude slower than the crystalline systems, as seen in Figure 1. The amorphous ML simulations have diffusion rates about 5 times slower than the crystalline systems. In addition, in both ML and CIP simulations, the Li concentration does not have a significant effect on diffusivity in amorphous LLZO, unlike in crystalline LLZO where certain concentrations are known to cause undesirable ordering.[22] For the CIP simulations of amorphous LLZO, there is little dependence on density compared to crystalline LLZO, with the amorphous diffusivity ranging from A-D_{CIP}^{CIP} = 4.8 × 10^{-7} to 8.0 × 10^{-7} cm^2/s and the crystalline diffusivity ranging from C-D_{CIP}^{CIP} = 3.61 × 10^{-6} to 2.94 × 10^{-5} cm^2/s at 1100 K. In contrast, the ML diffusivities generally have a strong dependence on cell density, particularly for the amorphous simulations, which exhibit sharp declines in A-D_{ML}^{ML} with increased density.

Figure 1B shows that the activation energy barriers for Li diffusion (E_a) largely match the trends in diffusivity, other than exceptions noted below. The activation energies were calculated for all systems assuming an Arrhenius relationship between the diffusivity and temperature. For both potentials, the experimental cell volume for the crystalline systems features an E_a which matches reasonably well with a comprehensive collection of LLZO experimental values of around 0.35 eV (C-E_a^{ML} = 0.25 eV, C-E_a^{CIP} = 0.29 eV).[14] Some underestimation of E_a is expected since grain boundaries and other microstructural features present in real experiments have been shown to raise the E_a in LLZO[14] yet are absent in our single-crystal simulations. Independent of potential, the E_a's are

https://doi.org/10.1021/acs.jpcc.4c00171
J. Phys. Chem. C XXXX, XXX, XXX−XXX

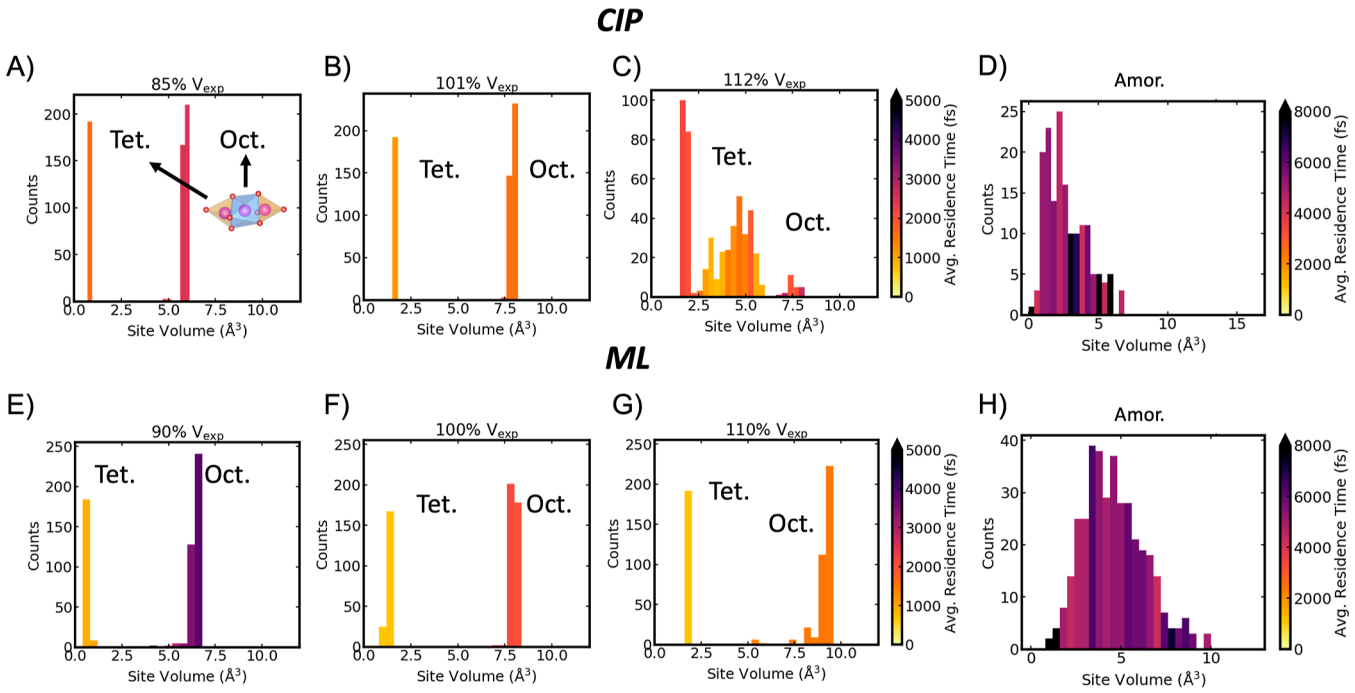

Figure 4. (A–D) Histograms of Li site volumes for CIP potentials calculated using Zeo++. A–C are the compressed, experimental, and expanded crystalline systems, respectively; D is an example amorphous simulation. (E–H) Histograms of Li site volumes for ML potentials. E–G are the compressed, experimental, and expanded crystalline systems, respectively; H is an example amorphous simulation. For all histograms, the color of the bar in the histograms corresponds to the average residence time of the sites within the volume range. The amorphous plots are representative of other amorphous Li concentrations and cell densities. Note the amorphous residence time scale bar extends to 8000 fs and the crystalline systems only extends to 5000 ps.

larger in amorphous simulations than in most of the crystalline systems. Crystalline simulations have very similar activation energies at the experimental volume and compressive strain, but diverge at expanded volumetric strain. The main difference between the two potentials is the trend of the crystalline C-E_a^{CIP}'s, which increases with expanded volumetric strain and has a sharp increase for two largest volumes tested, resulting in C-E_a^{CIP}'s similar to the amorphous CIP systems. When the cell is expanded from 107%V_{exp} (ρ = 4.74 g/cm^3) to 112%V_{exp} (ρ = 4.52 g/cm^3), the C-E_a^{CIP} nearly doubles. In contrast, the C-E_a^{ML}'s decreases with expanded volumetric strain, as do the ML amorphous simulations on average. The sharp increase in C-E_a^{ML} at 120%V_{exp} is due to the amorphization of the simulation cell, which is consistent with the flat trend in diffusivity at those densities.

Note that the smallest E_a does not always correlate with the largest diffusivity at a given temperature. For example, the CIP crystalline simulation at 1100 K with 107%V_{exp} (ρ = 4.74 g/cm^3) has the largest C-D_{CIP}^{CIP}, but the activation energy barrier is actually higher than at the experimental density. In this instance, the pre-exponential factor overcomes the increased barrier for migration. The pre-exponential (D_0 = maximum diffusion coefficient) is affected by many properties of the material, including jump frequency and success rate. At the experimental volume, Li has the most jumps and the highest fraction of "successful" jumps (jumps that do not result in a back jump), compared to other volumetric strains.

The trends with strain between CIP and ML for the amorphous simulations are different. The A-E_a^{CIP} for $Li_{6.25}$ increases as the volume is expanded, while the A-E_a^{CIP} is relatively flat for the $Li_{6.5}$ and $Li_{6.75}$ concentrations. In contrast, the A-E_a^{ML}'s decreases with expanded volumetric strain. To understand the differences in the trends with potential, we consider the amorphization, connectivity, and distribution of site volumes below.

Interatomic Potential Affects the Far-From Equilibrium Structures. To demonstrate the importance of connectivity of low-barrier diffusion pathways, the Li probability densities averaged over simulations at 1100 K are compared for the amorphous and crystalline systems. Figure 2 reveals the well-connected pathways in the crystalline systems with all sites having similar low-residence times (corresponding to rapid transport), as expected. The pathway consists of 24d tetrahedral sites bridged by two 96h octahedral sites which form rings interconnected by the 24d tetrahedral sites in both the ML and CIP simulations. The crystalline pathway allows for isotropic diffusion and is consistent with findings in previous studies.[34−36]

In the expanded CIP crystalline system, there are still many sites with high jump frequencies (yellow), but these are isolated from each other by regions with longer residence times, the cyan colored regions in Figure 2C. We describe these isolated regions as superbasins with fast diffusion within the basin (low residence times) but slow diffusion between basins, which impedes long-range diffusion. In contrast, the ML potentials expand uniformly and do not form superbasins. The expanded ML system includes some slow tetrahedral sites, in addition to many slow octahedral sites. Figure 2 shows how the Li density around the ML tetrahedral sites becomes expanded and elongated compared to the more compressed cells. The changes to the tetrahedral sites are quantified in the discussion of Figure 4.

Figure 2 shows there are still many sites with short residence times in the expanded CIP simulation. In addition to the

https://doi.org/10.1021/acs.jpcc.4c00171
J. Phys. Chem. C XXXX, XXX, XXX−XXX

Table 1. Diffusivity [cm^2/s] in Amorphous LLZO at 700 K with 112%V_{exp} (ρ = 4.52 g/cm^3) from a Computational Experiment that Uses a Different Potential to Generate the Structure than the One Used to Run the MD[a]

potential	D [cm^2/s] CIP structure	D/D_{CIP}^{CIP}	D [cm^2/s] ML structure	D/D_{CIP}^{CIP}
ML	A-D_{CIP}^{ML} = 2.24 × 10^{-7}	10.1:1	A-D_{ML}^{ML} = 3.88 × 10^{-7}	17.6:1
CIP	A-D_{CIP}^{CIP} = 2.21 × 10^{-8}	1:1	A-D_{ML}^{CIP} = 3.87 × 10^{-8}	1.75:1

[a]The D/D_{CIP}^{CIP} ratio is the given diffusivity over the slowest diffusivity.

Table 2. Volume, Activation Energy (E_a), and Diffusion Coefficient (D), at 1100 K are Given for Simulations in Which In-Depth Jump Analyses Will be Presented

CIP system	85%V crystal	101%V crystal	112%V crystal	112%V amorphous
E_a [eV]	0.27	0.29	0.56	0.61
D [cm^2 s^{-1}]	1.82 × 10^{-5}	2.88 × 10^{-5}	1.64 × 10^{-5}	5.60 × 10^{-7}
ML system	90%V crystal	100%V crystal	110%V crystal	112%V amorphous
E_a [eV]	0.26	0.25	0.17	0.48
D [cm^2 s^{-1}]	5.36 × 10^{-6}	1.36 × 10^{-5}	2.914 × 10^{-5}	5.68 × 10^{-6}

superbasins, there is a higher percentage of Li hopping into a site then quickly returning to the previous site (backjumps) in the expanded system (84% backjumps) when compared to the compressed (60% backjumps) and experimental density (64% backjumps) systems.

In both ML and CIP amorphous simulations, the diffusion pathway is fragmented with fewer percolation pathways for Li transport across the cell. There are only a few connected pathways visible. Figure 2D,H shows many slow individual sites and small site clusters (blue) isolated from superbasins or low barrier diffusion pathways (yellow-pink), especially in the CIP configuration. The formation of superbasins in amorphous systems is expected due to the distribution of sites with varying activation energy barriers.[37] The disrupted pathways and lack of a long-range isotropic percolation network in the amorphous simulation contributes to the reduced diffusivity. Li that get trapped have lower diffusivity compared to Li that diffuse along the connected percolating pathways. The connectivity of the pathways will be quantified with a GOP below.

To quantify the connectedness of the amorphous systems we employ a GOP.[33] We generate the graphs using the probability of Li jumping from one site, i, to another, j, then calculate the GOP. Lower, more negative GOP values indicate a more connected system. As seen in Figure 3 there is a direct relationship between higher connectedness and higher diffusivity in the ML structures compared to the CIP structures ("x"s versus squares). The CIP structures have GOP values around −100 and the ML structures have values around −250.

In addition to differences in connectedness, each potential causes differences in the local atomic environment, as measured by power spectrum and pair-distribution functions. The oxygen power spectrum indicates that there are softer oxygen phonon modes due to the CIP, while the pair distribution function shows slightly more structure at 4 Å in the CIP than the MLIP (Figure 3B,C). These differences in local environment can also contribute to the observed differences in diffusivity. The ML potential is more reliable in reproducing the power spectrum from DFT (Figure S9), on which it was trained.

Comparing the Effect of Amorphous Structure Versus Potential on Diffusivity. The following in-depth computational experiment was performed to distinguish the effect of the amorphous structure generated by each potential versus the effect of the potential itself. We ran MD at 700 K using the 111%V_{exp} (ρ = 4.52 g/cm^3) amorphous structure created by the classical potential with the ML interatomic potential and vice versa. The temperature (700 K) was chosen because it was the lowest temperature simulated and closest to room temperature. The ML structure gives slightly faster diffusivities, A-D_{ML}^{ML} and A-D_{ML}^{CIP}, than the diffusivities from the classical potential-derived structure, A-D_{CIP}^{CIP} and A-D_{CIP}^{ML}. The ML structure's higher diffusivities matches the higher connectivity as measured by the GOP. This result confirms that the atomic structure of the disordered configuration plays a role in the faster diffusivity of the ML simulations compared to the CIP.

Table 1 shows the "normal" ML diffusivity A-D_{ML}^{ML} is 17.6 times faster than the A-D_{CIP}^{CIP}, which is a larger difference than at 1100 K (10 times faster). However, the A-D_{CIP}^{ML} diffusivity is only 10.1 times larger than the A-D_{CIP}^{CIP}, which highlights the effect of slow classical structure.

This analysis also allows us to deconvolute the role of the potential choice in the description of the dynamics, independently of the respective effects on atomic structure. Thus, ignoring the effect of structure connectivity, we find the ML potentials are about 1 order of magnitude faster than the classical potentials. Thus, the potential itself seems to have a larger effect on diffusivity than the structure, though both factors are relevant. The following sections highlight the different aspects of the structures made from the classical potentials versus the machine learning potentials.

Site Analysis. In the following section we show how volumetric strain and amorphization affects diffusivity through calculating the relationship between Li site volume and site residence times. We use two methods to calculate site volume, the area enclosed by the static lattice using Zeo++[32] and the area explored by the Li ions using the Sitator package.[31] Table 2 highlights the diffusion coefficient for the simulations selected for comparison. Note that in the site networks for the crystalline systems, Sitator identified single Li octahedral sites, which correspond to the 48g sites, instead of the typical split octahedral sites (96h sites).

Correlation of Sites Volume Distribution and Diffusivity. The distribution of lithium site volumes is dependent on the volumetric strain, the crystallinity of the system, and the method of calculation. First we will describe the site volumes as calculated by Zeo++[32] using the static lattice. For ML and CIP, the compressed (Figure 4A) and experimental (Figure 4B) volumes of crystalline LLZO have a narrow distribution of

https://doi.org/10.1021/acs.jpcc.4c00171
J. Phys. Chem. C XXXX, XXX, XXX−XXX

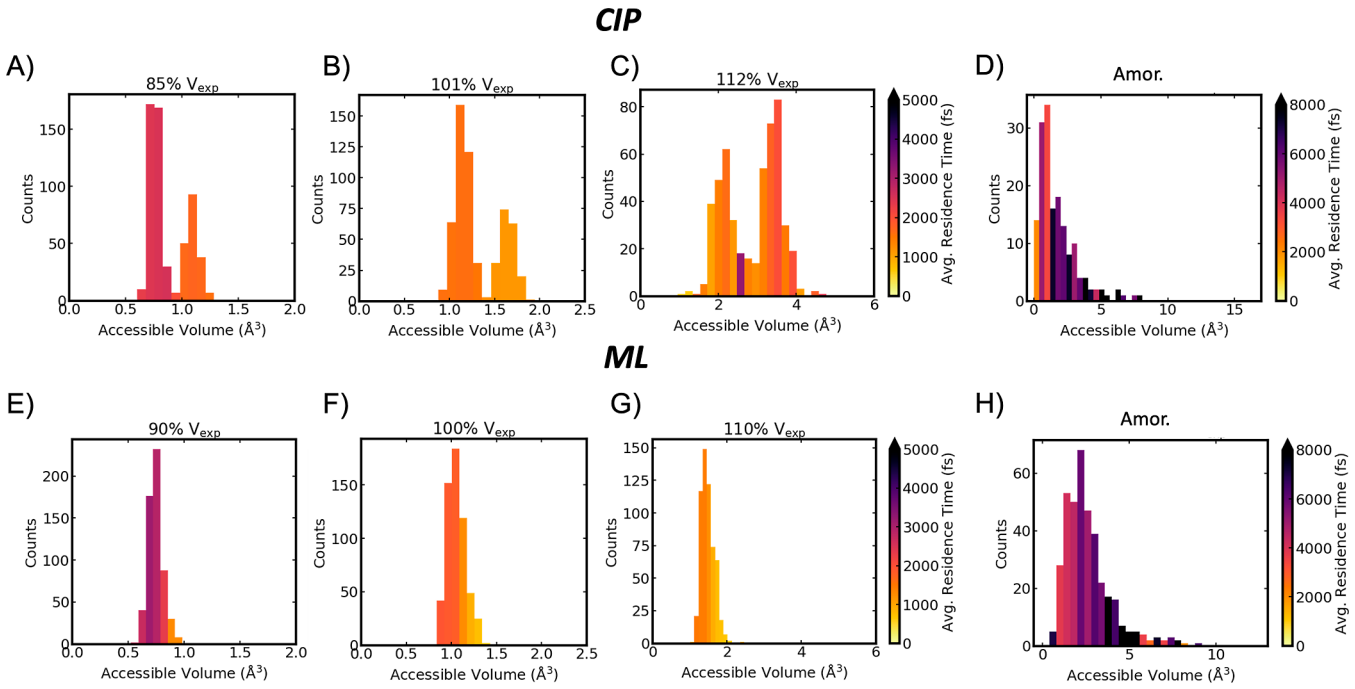

Figure 5. (A−D) Histograms of Li accessible site volumes calculated using volume explored by Li while occupying the site. (A)−(C) are the compressed, experimental, and expanded crystalline systems, respectively; (D) is an example amorphous. (E−H) Histograms of Li site volumes for ML potentials. E−G are the compressed, experimental, and expanded crystalline systems, respectively; H is an example amorphous system. For all histograms, the color of the bar in the histograms corresponds to the average residence time of the sites within the volume range. The amorphous plot is representative of other Li concentrations and cell densities. Note the amorphous residence time scale bar extends to 8000 fs and the crystalline systems only extends to 5000 ps.

site volumes for both the larger octahedral sites and the smaller tetrahedral sites. In LLZO, each tetrahedral site is connected to 4 other tetrahedral sites via octahedral sites; an example of the tet-oct-tet arrangement along the diffusion pathway is in the inset of Figure 4A. As expected, the sites in the compressed system are smaller, yet the smaller sites do not cause significantly slower diffusion or larger activation energy with either the CIP or ML potentials. In fact, Li in the smaller tetrahedral sites have lower residence times compared to the larger octahedral sites, consistent with neutron experiments and other computational studies.[36,38]

The site volume distributions for the expanded crystalline ML and CIP potentials differ from each other. The CIP distribution shows a significant spread in the octahedral sites while the ML distribution is narrower with only a few outlier sites. Based on Figure 2, we posit that slower diffusivity in the expanded CIP simulation was due to distorted sites, which is confirmed by the wide distribution of octahedral site volumes in Figure 4C. In the expanded crystalline system for both potentials, the tetrahedral sites retain a narrow distribution. In contrast to the compressed crystalline cells, the tetrahedral sites become the slow sites in the expanded CIP cell while the ML cell retains the faster tetrahedral sites.

Variations in the site volume distributions by potential show that selecting the potential is important, especially when simulating the nonequilibrium behavior or properties, like strain, even for crystalline systems. During the expansion of the crystalline cell, for the CIP potentials there is a nonuniform expansion of the sites at 112%V_{exp} (Figures 2 and 4C), while for the ML potentials the cell uniformly expands (Figures 2 and 4G). The nonuniform expansion of site volumes leads to much higher activation energy barriers for the Li to escape some sites, often resulting in slow sites with long residence times. In addition, if sites with high activation energy barriers surround a collection of sites with lower activation energy barriers, together they create a superbasin which impedes long-range diffusion of Li, as defined above. In expanded simulations, while we see more jumps, a higher percentage of those jumps are back-jumps, which is a hallmark of Li jumping inside the superbasin rather than along diffusion pathways. We determine that the nonuniform expansion in the CIP systems causes superbasins and slow sites, since the sites expand uniformly for the ML potentials together with increasing diffusivity, until amorphization of the cell at sufficiently expansive strain 120%V_{exp} (ρ = 4.21 g/cm^3).

In both CIP and ML simulations, the amorphous cells have a wide distribution of sites, with some CIP site volumes that are much larger than in the expanded crystalline cells. For both potentials, amorphization disrupts the percolation network of diffusion pathways with low activation energy barriers through distorting sites, as plotted in Figure 2 and quantified in Figure 3 by the GOP.

Comparison of amorphous systems generated with the same potential shows that different densities and Li stoichiometries have qualitatively similar site volumes and residence times. We present these other amorphous simulation site distributions, including other temperatures, in the Supporting Information. We hypothesize that since the amorphous structures already have disrupted networks, the effect of further disruption (strain or stoichiometry) on site volume distributions is less pronounced compared to crystalline. However, strain has more systematic effect on diffusivity with the ML potential compared to CIP: A-D_{ML}^{ML} decreases with compressive strain while A-D_{CIP}^{CIP} does not. Thus, some variability in the nature of

https://doi.org/10.1021/acs.jpcc.4c00171
J. Phys. Chem. C XXXX, XXX, XXX−XXX

the structural disordering is evident even in the ML amorphous diffusivity, even if there are no differences in the site volumes or residence times with strain. It is also worth noting that the trends for amorphous and low-density crystalline tend to converge in Figure 1 (especially the E_a values), which implies that the character and/or effect of the atomic structural disruption is analogous for both far from equilibrium strain and amorphization.

In summary, the effect of strain on jumps and site volumes in the crystalline simulations can be significant; in Figure 4 we show that the expanded and compressed simulations can increase residence times by ∼1 ps compared to crystalline experimental volume at 1100 K for both potentials. The effects of disorder (amorphization) are even more significant in raising some residence times to over 8 ps.

Insights from Li Site Exploration Versus Static Site Volumes. In addition to static site volume we also investigate the accessible site volume, which is the volume explored by Li when occupying the site in Figure 5. Comparing the site volumes and accessible volume show the explored volume of the Li is very different from the static site volume. In the CIP simulations the Li explore most of the tetrahedral site volume, but a much smaller percentage of the octahedral site volume, such that the accessible volume of the octahedral sites is actually smaller than the tetrahedral site. Since the volume explored by the Li is small, compressing the octahedral site does not significantly change the diffusivity. The residence times increase for both octahedral and tetrahedral sites when the cell is compressed but fewer backjumps negate the slowing effect of longer site residence times such that the diffusivity (C-D_{CIP}^{CIP}) is not significantly affected.

In contrast to the CIP simulations, the accessible site volumes in the ML simulations do not have separate distributions for the octahedral and tetrahedral sites; instead site exploration has a fairly normal distribution. The average ML accessible volume is similar to the average tetrahedral site volume in Figure 4E. These similar site volumes correlate with the smaller activation energy barrier in the ML simulations. This similarity shows that the Li do not explore all of the larger octahedral site volume in the ML simulations, like in the CIP simulations.

For the amorphous simulations, there is not much difference between the site volume distributions using the Zeo++[32] and static lattice algorithm or the accessible site volume with Sitator for the ML potential. For each site in the amorphous simulation, we divide the accessible site volume by the static site volume. The average of that ratio is 51% for the CIP amorphous simulation and 86% for the ML amorphous simulation. Since A-D_{CIP}^{CIP} is an order of magnitude smaller than the A-D_{ML}^{ML}, it is likely that the larger static site volumes are an indication of super basins that disrupt the percolation network in the A-CIP simulations.

CONCLUSIONS

We found that for the crystalline simulations at the experimental volume, both ML and classical potentials give very similar results for diffusivity and diffusion mechanism. In contrast, the potentials behave differently with volumetric strain that creates far from equilibrium crystalline structures or amorphized systems. The two different potentials created unique local disorder and disruptions of the percolation pathways, which were quantified using static and Li explored site volumes and the GOP. The MD simulations showed that choice of potential led to orders of magnitude differences in the diffusivity in the far from equilibrium structures.

We now speculate on the differences in Li diffusivity between the CIP and ML potential. Our computational experiments of running MD with a different potential than the one that generated the amorphous structure (A-D_{CIP}^{ML} and A-D_{ML}^{CIP}) allow us to deconvolute the effects of the aforementioned structural disorder and the dynamical description of diffusivity, as manifested differently in the two potentials. We showed that the classical amorphous structure is slower than the ML amorphous structure. In addition, the classical potential is inherently slower than the machine learning potential, likely due to the hardness of the oxygen phonon modes (see Figure 3B and our previous publication[19]). In addition, the difference in octahedral/tetrahedral site volumes as explored by the Li ions can be explained by the harder oxygen phonon modes in the CIP simulations compared to the ML. In the CIP simulations the harder oxygen modes bounce the Li around the site more causing the Li to explore more of the site. While in the ML simulations the absence of the harder modes allow Li to stay closer to its equilibrium lattice position and explore less of the site.

The additional exploration of site volume in the CIP simulations could lead to fewer jump attempts and thus the slower diffusivity observed in the CIP versus ML potentials. A previous investigation using the same CIP showed that Li concentrations of x = 7, 6, 4, 3 in $Li_xLa_3Zr_2O_{12}$ lead to symmetric Li configurations on the Li sublattice, which slows diffusion, while noninteger Li concentrations have higher diffusivity because the lack of symmetry in the Li configuration leads to frustration that enhances diffusion.[22] We hypothesize that the expanded system is alleviating some of the beneficial frustration by allowing larger displacement within each site. Increased backjumps and a larger site exploration may explain some of the longer residence times in the expanded CIP system. Also the larger volumetric strain may reduce Li−Li Coulombic repulsion, which would then lower jump attempts. Note, the CIP MD were able to simulate the cubic to tetragonal phase transition and effect of Li stoichiometry on the diffusivity. The ML potential was trained on ab initio MD simulations of both the cubic crystalline, tetragonal crystalline, and amorphous structures and reproduced the ab initio MD very well, especially the phonon modes (Figure S9).

In conclusion, we caution researchers when using either classical potentials or ML potentials to explore nonequilibrium phase space. The ML is constrained by the ab initio training set and the classical is constrained by the properties that were used to train and validate the classical potential. It is possible that the ab initio MD was not able to generate enough different strained amorphous configurations to generate some of the very disordered structures accessed by the classical potential. To simulate densities far from equilibrium and amorphous or defective structures, care must be taken to train a potential and make sure that the input or properties reflect reality. Collaborations with experimental groups will accelerate the development of ML potentials for far from equilibrium structures.

ASSOCIATED CONTENT

Supporting Information

The Supporting Information is available free of charge at https://pubs.acs.org/doi/10.1021/acs.jpcc.4c00171.

https://doi.org/10.1021/acs.jpcc.4c00171
J. Phys. Chem. C XXXX, XXX, XXX−XXX

Figures showing analyses of all the simulations; details of the ML potential validation (PDF)

AUTHOR INFORMATION

Corresponding Author

Nicole Adelstein − *Department of Chemistry & Biochemistry, San Francisco State University, San Francisco, California 94132, United States;* orcid.org/0000-0002-7491-9592; Email: nicoleal@sfsu.edu

Authors

Andrew C. Grieder − *Department of Materials Science and Engineering, University of Wisconsin-Madison, Madison, Wisconsin 53715, United States;* orcid.org/0000-0003-4952-7279

Kwangnam Kim − *Materials Science Division, Lawrence Livermore National Laboratory, Livermore, California 94550, United States;* orcid.org/0000-0003-1149-1733

Liwen F. Wan − *Materials Science Division, Lawrence Livermore National Laboratory, Livermore, California 94550, United States;* orcid.org/0000-0002-5391-0804

James Chapman − *Department of Mechanical Engineering, Boston University, Boston, Massachusetts 02215, United States;* orcid.org/0000-0001-8451-0275

Brandon C. Wood − *Materials Science Division, Lawrence Livermore National Laboratory, Livermore, California 94550, United States;* orcid.org/0000-0002-1450-9719

Complete contact information is available at: https://pubs.acs.org/10.1021/acs.jpcc.4c00171

Notes

The authors declare no competing financial interest.

ACKNOWLEDGMENTS

The work by K.K., L.F.W., and B.C.W. was performed under the auspices of the U.S. Department of Energy by Lawrence Livermore National Laboratory (Contract no. DE-AC52-07NA27344) and was sponsored by the Office of Energy Efficiency and Renewable Energy, Vehicle Technologies Office, through the Battery Materials Research Program. K.K., L.F.W., and B.C.W. acknowledge an award of computer time by the Innovative and Novel Computational Impact on Theory and Experiment (INCITE) program via the Argonne Leadership Computing Facility, which is a DOE Office of Science User Facility supported under Contract no. DE-AC02-06CH11357. J.C. acknowledges the support from the College of Engineering and Department of Mechanical Engineering at Boston University. The work of A.G. and N.A. was supported by the National Science Foundation under grant no. DMR-1710630, and simulations utilized the Extreme Science and Engineering Discovery Environment (XSEDE) Stampede2 at the University of Texas, Austin, through allocation DMR180033. We would like to thank Maria A. Gomez and Conrad Gomez-Haibach for insightful discussions.

REFERENCES

(1) Grady, Z. A.; Wilkinson, C. J.; Randall, C. A.; Mauro, J. C. Emerging Role of Non-Crystalline Electrolytes in Solid-State Battery Research. *Front. Energy Res.* **2020**, *8*, 218.

(2) Ding, J.; Ji, D.; Yue, Y.; Smedskjaer, M. M. Amorphous Materials for Lithium-Ion and Post-Lithium-Ion Batteries. *Small* **2023**, *20*, 2304270.

(3) Luntz, A. C.; Voss, J.; Reuter, K. Interfacial Challenges in Solid-State Li Ion Batteries. *J. Phys. Chem. Lett.* **2015**, *6*, 4599−4604.

(4) Han, F.; Westover, A. S.; Yue, J.; Fan, X.; Wang, F.; Chi, M.; Leonard, D. N.; Dudney, N. J.; Wang, H.; Wang, C. High Electronic Conductivity as the Origin of Lithium Dendrite Formation within Solid Electrolytes. *Nat. Energy* **2019**, *4*, 187−196.

(5) Jinnouchi, R.; Karsai, F.; Kresse, G. On-the-Fly Machine Learning Force Field Generation: Application to Melting Points. *Phys. Rev. B* **2019**, *100*, 014105.

(6) Singraber, A.; Morawietz, T.; Behler, J.; Dellago, C. Parallel Multistream Training of High-Dimensional Neural Network Potentials. *J. Chem. Theory Comput.* **2019**, *15*, 3075−3092.

(7) Buschmann, H.; Dölle, J.; Berendts, S.; Kuhn, A.; Bottke, P.; Wilkening, M.; Heitjans, P.; Senyshyn, A.; Ehrenberg, H.; Lotnyk, A.; et al. Structure and Dynamics of the Fast Lithium Ion Conductor "$Li_7La_3Zr_2O_{12}$". *Phys. Chem. Chem. Phys.* **2011**, *13*, 19378−19392.

(8) Murugan, R.; Thangadurai, V.; Weppner, W. Fast Lithium Ion Conduction in Garnet-Type $Li_7La_3Zr_2O_{12}$. *Angew. Chem., Int. Ed.* **2007**, *46*, 7778−7781.

(9) Wolfenstine, J.; Sakamoto, J.; Allen, J. L. Electron Microscopy Characterization of Hot-Pressed Al Substituted $Li_7La_3Zr_2O_{12}$. *J. Mater. Sci.* **2012**, *47*, 4428−4431.

(10) Hoinkis, N.; Schuhmacher, J.; Fuchs, T.; Leukel, S.; Loho, C.; Roters, A.; Richter, F. H.; Janek, J. Amorphous Phase Induced Lithium Dendrite Suppression in Glass-Ceramic Garnet-Type Solid Electrolytes. *ACS Appl. Mater. Interfaces* **2023**, *15*, 28692−28704.

(11) Wang, C.; Fu, K.; Kammampata, S. P.; McOwen, D. W.; Samson, A. J.; Zhang, L.; Hitz, G. T.; Nolan, A. M.; Wachsman, E. D.; Mo, Y.; et al. Garnet-Type Solid-State Electrolytes: Materials, Interfaces, and Batteries. *Chem. Rev.* **2020**, *120*, 4257−4300.

(12) Sharafi, A.; Haslam, C. G.; Kerns, R. D.; Wolfenstine, J.; Sakamoto, J. Controlling and Correlating the Effect of Grain Size with the Mechanical and Electrochemical Properties of $Li_7La_3Zr_2O_{12}$ Solid-State Electrolyte. *J. Mater. Chem. A* **2017**, *5*, 21491−21504.

(13) Garbayo, I.; Struzik, M.; Bowman, W. J.; Pfenninger, R.; Stilp, E.; Rupp, J. L. M. Glass-Type Polyamorphism in Li-Garnet Thin Film Solid State Battery Conductors. *Adv. Energy Mater.* **2018**, *8*, 1702265.

(14) Heo, T. W.; Grieder, A.; Wang, B.; Wood, M.; Hsu, T.; Akhade, S. A.; Wan, L. F.; Chen, L.-Q.; Adelstein, N.; Wood, B. C. Microstructural Impacts on Ionic Conductivity of Oxide Solid Electrolytes from a Combined Atomistic-Mesoscale Approach. *npj Comput. Mater.* **2021**, *7*, 214.

(15) Yu, S.; Siegel, D. J. Grain Boundary Contributions to Li-Ion Transport in the Solid Electrolyte $Li_7La_3Zr_2O_{12}$(LLZO). *Chem. Mater.* **2017**, *29*, 9639−9647.

(16) Dawson, J. A.; Canepa, P.; Famprikis, T.; Masquelier, C.; Islam, M. S. Atomic-Scale Influence of Grain Boundaries on Li-Ion Conduction in Solid Electrolytes for All-Solid-State Batteries. *J. Am. Chem. Soc.* **2018**, *140*, 362−368.

(17) Shiiba, H.; Zettsu, N.; Yamashita, M.; Onodera, H.; Jalem, R.; Nakayama, M.; Teshima, K. Molecular Dynamics Studies on the Lithium Ion Conduction Behaviors Depending on Tilted Grain Boundaries with Various Symmetries in Garnet-Type $Li_7La_3Zr_2O_{12}$. *J. Phys. Chem. C* **2018**, *122*, 21755−21762.

(18) Fu, S.; Arinicheva, Y.; Hüter, C.; Finsterbusch, M.; Spatschek, R. Grain Boundary Characterization and Potential Percolation of the Solid Electrolyte LLZO. *Batteries* **2023**, *9*, 222.

(19) Kim, K.; Dive, A.; Grieder, A.; Adelstein, N.; Kang, S.; Wan, L. F.; Wood, B. C. Flexible Machine-Learning Interatomic Potential for Simulating Structural Disordering Behavior of $Li_7La_3Zr_2O_{12}$ Solid Electrolytes. *J. Chem. Phys.* **2022**, *156*, 221101.

(20) Plimpton, S. Fast Parallel Algorithms for Short-Range Molecular Dynamics. *J. Comput. Phys.* **1995**, *117*, 1−19.

(21) Singraber, A.; Behler, J.; Dellago, C. Library-Based LAMMPS Implementation of High-Dimensional Neural Network Potentials. *J. Chem. Theory Comput.* **2019**, *15*, 1827−1840.

(22) Kozinsky, B.; Akhade, S. A.; Hirel, P.; Hashibon, A.; Elsässer, C.; Mehta, P.; Logeat, A.; Eisele, U. Effects of Sublattice Symmetry

and Frustration on Ionic Transport in Garnet Solid Electrolytes. *Phys. Rev. Lett.* **2016**, *116*, 055901.
(23) Bush, T. S.; Gale, J. D.; Catlow, C. R. A.; Battle, P. D. Self-Consistent Interatomic Potentials for the Simulation of Binary and Ternary Oxides. *J. Mater. Chem.* **1994**, *4*, 831.
(24) Woodley, S. M.; Battle, P. D.; Gale, J. D.; Catlow, R. A. The Prediction of Inorganic Crystal Structures using a Genetic Algorithm and Energy Minimisation. *Phys. Chem. Chem. Phys.* **1999**, *1*, 2535−2542.
(25) Behler, J.; Parrinello, M. Generalized Neural-Network Representation of High-Dimensional Potential-Energy Surfaces. *Phys. Rev. Lett.* **2007**, *98*, 146401.
(26) Mottet, M.; Marcolongo, A.; Laino, T.; Tavernelli, I. Doping in Garnet-Type Electrolytes: Kinetic and Thermodynamic Effects from Molecular Dynamics Simulations. *Phys. Rev. Mater.* **2019**, *3*, 035403.
(27) Kaneko, M.; Ninomiya, K.; Hishida, T.; Takeuchi, Y.; Otani, K.; Nishibori, M. Enhanced Li-Ion Conductivity of Strontium Doped Li-Excess Garnet-Type $Li_{7+x}La_{3-x}Sr_xZr_2O_{12}$. *J. Am. Ceram. Soc.* **2023**, *106*, 4480−4487.
(28) Jakse, N.; Pasturel, A. Glass Forming Ability and Short-Range Order in a Binary Bulk Metallic Glass by Ab Initio Molecular Dynamics. *Appl. Phys. Lett.* **2008**, *93*, 113104.
(29) Smith, J. G.; Siegel, D. J. Low-Temperature Paddlewheel Effect in Glassy Solid Electrolytes. *Nat. Commun.* **2020**, *11*, 1483.
(30) Vollmayr, K.; Kob, W.; Binder, K. Cooling-Rate Effects in Amorphous Silica: A Computer-Simulation Study. *Phys. Rev. B* **1996**, *54*, 15808−15827.
(31) Kahle, L.; Musaelian, A.; Marzari, N.; Kozinsky, B. Unsupervised Landmark Analysis for Jump Detection in Molecular Dynamics Simulations. *Phys. Rev.* **2019**, *3*, 055404.
(32) Willems, T. F.; Rycroft, C. H.; Kazi, M.; Meza, J. C.; Haranczyk, M. Algorithms and Tools For High-Throughput Geometry-Based Analysis of Crystalline Porous Materials. *Microporous Mesoporous Mater.* **2012**, *149*, 134−141.
(33) Chapman, J.; Goldman, N.; Wood, B. C. Efficient and Universal Characterization of Atomic Structures through a Topological Graph Order Parameter. *npj Comput. Mater.* **2022**, *8*, 37.
(34) He, X.; Zhu, Y.; Mo, Y. Origin of Fast Ion Diffusion in Super-Ionic Conductors. *Nat. Commun.* **2017**, *8*, 15893.
(35) Meier, K.; Laino, T.; Curioni, A. Solid-State Electrolytes: Revealing the Mechanisms of Li-Ion Conduction in Tetragonal and Cubic LLZO by First-Principles Calculations. *J. Phys. Chem. C* **2014**, *118*, 6668−6679.
(36) Jalem, R.; Yamamoto, Y.; Shiiba, H.; Nakayama, M.; Munakata, H.; Kasuga, T.; Kanamura, K. Concerted Migration Mechanism in the Li Ion Dynamics of Garnet-Type $Li_7La_3Zr_2O_{12}$. *Chem. Mater.* **2013**, *25*, 425−430.
(37) de Souza, V. K.; Wales, D. J. Energy Landscapes for Diffusion: Analysis of Cage-Breaking Processes. *J. Chem. Phys.* **2008**, *129*, 164507.
(38) Chen, Y.; Rangasamy, E.; Liang, C.; An, K. Origin of High Li^+ Conduction in Doped $Li_7La_3Zr_2O_{12}$ Garnets. *Chem. Mater.* **2015**, *27*, 5491−5494.

https://doi.org/10.1021/acs.jpcc.4c00171
J. Phys. Chem. C XXXX, XXX, XXX−XXX